SOILS AND FOUNDATIONS Vol. 51, No. 5, 835–847, Oct. 2011
Japanese Geotechnical Society

A SIMPLIFIED IMAGE ANALYSIS METHOD TO STUDY LNAPL MIGRATION IN POROUS MEDIA

GIANCARLO FLORES[i], TAKESHI KATSUMI[ii], TORU INUI[iii] and MASASHI KAMON[iv]

ABSTRACT

A novel Simplified Image Analysis Method was developed and tested to assess the saturation distribution values for water and LNAPLs (Light Non-Aqueous Phase Liquids) in granular soils subjected to fluctuating groundwater conditions. This method, based on the Beer-Lambert Law of transmissivity, determines the saturation of water (S_w) and LNAPLs (S_o) by comparing the average optical densities (D_i) for each matrix element of the tested domain to the corresponding average optical densities for three base pictures of the same domain taken with two digital cameras attached to two different band-pass filters ($\lambda = 450$ nm and 640 nm). Two equations with two unknowns (S_w and S_o) are defined for each mesh element, which enables the saturation distribution to be calculated under dynamic conditions. The three base conditions for the domain are: (i) fully saturated with water (D_i^{10}), (ii) fully saturated with LNAPL (D_i^{01}), and (iii) completely dry (D_i^{00}). The Simplified Image Analysis Method was then applied to analyze the behavior of two fluctuating groundwater systems, namely, two-phase air-water and three-phase air-water-LNAPL, in a one-dimensional column, $3.5 \times 3.5 \times 50$ cm, filled with Toyoura sand. The mass balance of the drainage-imbibition three-phase air-water-LNAPL system showed a difference of just 4.7% in LNAPL, demonstrating that this non-intrusive and non-destructive method is reliable for providing water and LNAPL saturation distributions throughout the domain when studying the effects of porous soil contamination by LNAPLs subjected to dynamic conditions.

Key words: contamination, fluctuating groundwater, image analysis, LNAPL, paraffin liquid, porous media, saturation (**IGC**: D3)

INTRODUCTION

Due to its accessibility, water for human consumption was originally obtained from surface water (rivers and lakes). Over time, however, groundwater has become the major source because of its stability as a water source (unlike surface water, groundwater is not easily affected by climatic conditions), its wide distribution, and its fairly good quality (Kiely, 1998). Unfortunately, groundwater often contains various contaminants, ranging from synthetic organic compounds and hydrocarbons to pathogens and radionuclides, caused mainly by human activities. Even worse, due to the slow velocity of groundwater within the hydrologic cycle, contamination tends to be long-term and localized; even after the pollution sources have been removed, self-purification of the aquifer still requires decades or centuries.

Depending on the densities, the aforementioned contaminants are either soluble or insoluble in water. Soluble contaminants, such as salts, dissolve in the groundwater and travel with it as a mixture without interface. However, insoluble contaminants form a physical interface with water, and they are prevented from mixing with the water. When the latter types of contaminants are lighter than water, such as hydrocarbons, they are called Light Non-Aqueous Phase Liquids (LNAPLs). LNAPLs float on top of aquifers and typically spread over them as thin films. In contrast, when they are heavier than water, such as chlorinated solvents, they are called Dense Non-Aqueous Phase Liquids (DNAPLs). DNAPLs tend to sink to the bottom of aquifers following the slopes of the confining layers (Fig. 1). The fate, the flow, and the transport of NAPLs are governed by complex interactions among capillary, viscous, and gravitational forces as well as by the mass transfer between phases and chemical and biological reactions. These processes are affected by factors such as temperature, soil and fluid compressibility, soil heterogeneity, the volume of the spilled NAPL, and the geometry of the spill source (Kamon et al., 2007).

To remediate LNAPL-contaminated sites in an efficient and cost-effective manner, a complete understanding of the contaminant behavior is essential. Thus, accurate numerical models based on and compared to

[i] Lecturer, Graduate School of Engineering, Kyoto University, Kyoto, Japan (flores.giancarlo.3v@kyoto-u.ac.jp).
[ii] Professor, Graduate School of Global Environmental Studies, Kyoto University, Kyoto, Japan (katsumi.takeshi.6v@kyoto-u.ac.jp).
[iii] Associate Professor, ditto (inui.toru.3v@ kyoto-u.ac.jp).
[iv] President, Kagawa National College of Technology, Kagawa, Japan.
The manuscript for this paper was received for review on February 4, 2010; approved on May 20, 2011.
Written discussions on this paper should be submitted before May 1, 2012 to the Japanese Geotechnical Society, 4-38-2, Sengoku, Bunkyo-ku, Tokyo 112-0011, Japan. Upon request the closing date may be extended one month.

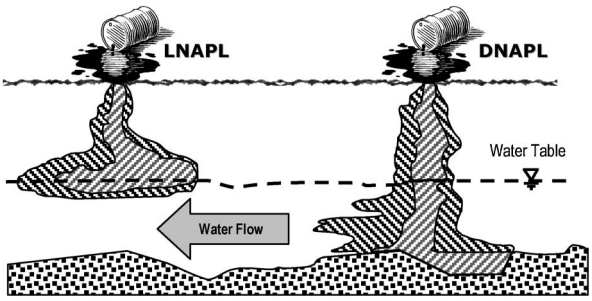

Fig. 1 LNAPL and DNAPL spill plumes

valid quantitative laboratory experiments should be developed. These experiments, in turn, should be able to provide the correct constitutive relations among pressure, saturation, and relative permeability (*k-S-p*), because these factors are used to solve the governing equations of multiphase flow. Van Genuchten (1980) developed a relatively simple equation relating relative permeability to saturation, which prompted other researchers to obtain the simpler saturation-pore pressure (*S-p*) relation to fully characterize multiphase flow (Høst-Madsen and Jensen, 1992; Van Geel and Sykes, 1994; Rimmer et al., 1998; Kechavarzi et al., 2000; Kamon et al., 2003; Sharma and Mohamed, 2003). Pore pressure measurements are simple. Some researchers rely on mechanical set-ups that manually increase suction values (Høst-Madsen and Jensen, 1992; Sharma and Mohamed, 2003), while others use pressure transducers (Van Geel and Sykes, 1994; Rimmer et al., 1998; Kechavarzi et al., 2000; Kamon et al., 2003).

There is not one single prevalent technique for measuring saturation, and those that currently exist can be roughly divided into two categories, namely, simple intrusive/destructive methods, such as gravimetric sampling, and very complex and usually expensive non-intrusive/non-destructive methods, such as gamma-ray (Tuck et al., 1998) or high-speed X-ray attenuation (DiCarlo et al., 1997) or electrical conductivity probes (Kamon et al., 2003). Unfortunately, the former do not allow saturation values to be monitored under dynamic conditions, and the latter are unable to simultaneously monitor the entire domain.

Thus, a simple and economic method, which can continuously measure the saturation distribution values as well as variations with time, is necessary for studying the effects of water fluctuation on LNAPL contaminants when spilled into the subsoil under controlled laboratory conditions. This new method should be (i) economical and easily calibrated to allow experiments to be conducted under different controlled conditions, (ii) non-intrusive and non-destructive to enable continuous tests under dynamic conditions without stopping the experiments to obtain saturation values, and (iii) able to simultaneously monitor the entire domain to allow for complete contamination characterization as well as direct comparisons with various numerical and mathematical models.

Herein, we propose a Simplified Image Analysis Method as a laboratory tool capable of fulfilling all of the above requirements. We anticipate that it will be a valuable instrument, which will aid in the understanding of LNAPL migration into the subsoil as well as address its effects when contaminating groundwater.

BACKGROUND

Saturation Measurement via Optical Methods

Among the non-intrusive/non-destructive methods mentioned in the previous section, the optical methods can continuously monitor the entire domain because equipment capable of recording visible, near-IR, or near-UV spectrum light is employed. Therefore, optical methods are better suited for studying systems subjected to dynamic conditions.

Schincariol et al. (1993) have correlated the optical density of scanned photographs with concentrations of NaCl solutions dyed with a tracer during miscible two-dimensional experiments. Their research suggests that the dye was theoretically acting as a true optical filter. The method enabled them to obtain a full-field analysis and to continuously monitor the distribution of and the variation in NaCl concentrations. Schincariol proposed a linear relation between optical density and saturation, but found that a quadratic relation has a better R^2 value; larger errors were found at lower saturations.

Darnault et al. (1998) have developed another method whereby the intensity of transmitted light through a thin two-dimensional flume is digitally recorded, and the water saturation in two-phase NAPL–water experiments is correlated to the average hue value of the pixels. The disadvantages of this method are the thin flume and the fact that a translucent porous medium must be employed.

In contrast, Kechavarzi et al. (2000) have proposed a method to measure the saturation of two fluids (water and NAPL) in a three-phase system. Similar to Schincariol et al. (1993), Kechavarzi et al. (2000) found a linear relationship between optical density and water saturation as well as between optical density and NAPL saturation. Thus, they proposed a combined linear relationship for samples containing both water and NAPL. If two pictures are taken at different wavelengths for each sample, then two linear relationships among optical density, water saturation, and NAPL saturation would be found. For the same experimental conditions, the two unknowns, S_w and S_o, could be described by two equations, as long as the values of the parameters in the linear relationships are known.

Extension of the Beer-Lambert Law of Transmittance

The Beer-Lambert Law of Transmittance states that when a beam of parallel monochromatic radiation with power I_0 strikes a block of absorbing matter perpendicular to the surface (Fig. 2), after passing through a material with length b, its power decreases to I_t due to absorption. The Beer-Lambert Law of Transmittance, an expression relating the initial radiant power and the transmitted power, can be written as

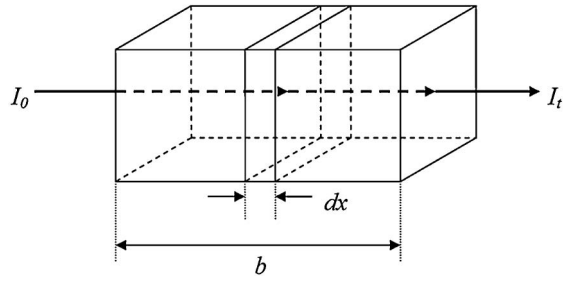

Fig. 2 Radiation with initial radiant power (I_0) is attenuated to transmitted power (I_t) by absorbing solution with path length of b centimeters

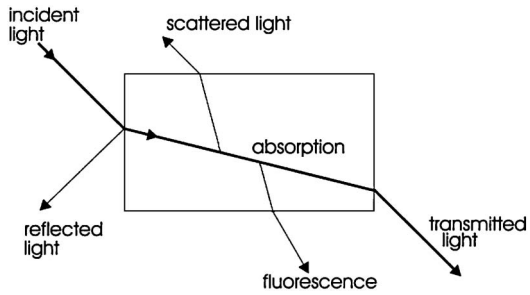

Fig. 3 Interaction of light with transparent material (Tilley, 2003)

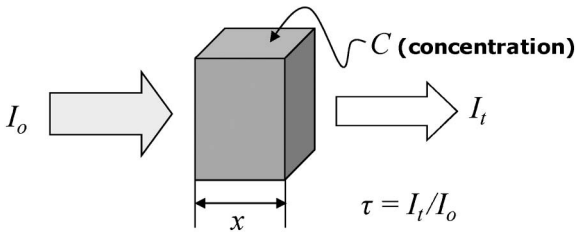

Fig. 4 Relation between initial (I_o) and final intensity (I_t) for light passing through dye with concentration C and thickness x

$$\log_{10}\frac{I_0}{I_t}=\varepsilon bM=D \tag{1}$$

where I_0 and I_t are the initial radiant power and the transmitted power, respectively. ε is a numerical constant, b is the length of the path, M is the number of moles per liter of absorbing solution, and D is the optical density (Skoog et al., 2007).

When a photographic film is subjected to light and subsequently developed, the exposed grains of silver halides are changed into metallic silver, creating a change in the light transmittance of the film (Iizuka, 1987). Transmittance τ defines how much light is transmitted through a photographic negative and can be expressed as

$$\tau=\frac{I_t}{I_0} \tag{2}$$

where I_t and I_0 are the transmitted and the incident luminous intensities, respectively (Fig. 3). In digital photography, RAW files are equivalent to photographic films, and the pixel value is equivalent to the transmitted light through a negative grain.

Optical density D is related to the transmittance as

$$D=-\log_{10}(\tau) \tag{3}$$

The value $D=0$, or unit transmittance, is the analogue for the reflectance of an ideal white surface (Gold and Asher, 1976).

For digital images, the average optical density D_i for a given spectral band i, is defined for the reflected light intensity as

$$D_i=\frac{1}{N}\sum_{j=1}^{N}d_{ji}=\frac{1}{N}\sum_{j=1}^{N}\left(-\log_{10}\left(\frac{I_{ji}^{r}}{I_{ji}^{0}}\right)\right) \tag{4}$$

where N is the number of pixels contained in the area of interest and d_{ji} is the optical density of the individual pixels. I_{ji}^{r} is the intensity of the reflected light given by the individual pixel values and I_{ji}^{0} is the intensity of the light that would be reflected by an ideal white surface (Kechavarzi et al., 2000).

For a sample with thickness x (Fig. 4), using the definition of transmittance (Eqs. (1) and (2)), the Beer-Lambert Law of Transmittance (Eq. (1)) can be rewritten as

$$\tau=e^{-aCx} \tag{5}$$

where τ is the transmittance of a solution with unit concentration, a is the absorption coefficient, C is the dye concentration, and x is the thickness of the medium (MacAdam, 1981).

Calculating the logarithm of Eq. (5) and using Eq. (3) yields

$$D=C\cdot D_0 \tag{6}$$

where D_0 is the optical density of a solution with unit concentration and D the optical density of a solution of concentration C. Equation (6) shows that the optical density is linearly correlated to the dye concentration, which has been experimentally confirmed by Kechavarzi et al. (2000) and by Flores et al. (2009a, b).

Multispectral Image Analysis Method

Employing two cameras with two different band-pass filters (wavelengths $\lambda=i$ and j) and mixing water and NAPL with dyes, whose predominant color wavelengths are i and j, the following two different sets of linear equations can be solved for S_w and S_o:

$$\begin{cases}D_i=a\cdot S_w+b\cdot S_o+c\\ D_j=d\cdot S_w+e\cdot S_o+f\end{cases} \tag{7}$$

This is the basis of the Multispectral Image Analysis Method, namely, the calculation of two correlation equations via calibration tests using small samples and their subsequent use to determine water and NAPL saturation values (S_w and S_o) for larger three-phase (air/water/NAPL) domains (Kechavarzi et al., 2000). Calculating the coefficients of both correlation equations is a time-consuming process (Flores et al., 2009b) that yields a unique pair of equations, which is later used to calculate water and NAPL saturation values (S_w and S_o) throughout a column or a tank via an indirect method called im-

age subtraction. The purpose of image subtraction is to compensate for spatial variations in lighting conditions; it is based on comparing the difference between the average optical densities at any given time (D_i and D_j) and those at the beginning of the tests when the initial saturation values (S_w and S_o) are known. The basic pair of equations is obtained from Eq. (7) by subtracting the values corresponding to the initial conditions

$$\begin{cases} \Delta D_i = a \cdot \Delta S_w + b \cdot \Delta S_o \\ \Delta D_j = d \cdot \Delta S_w + e \cdot \Delta S_o \end{cases} \quad (8)$$

where

$$\begin{cases} \Delta D_i = D_i - D_i^0 \\ \Delta D_j = D_j - D_j^0 \\ \Delta S_w = S_w - S_w^0 \\ \Delta S_o = S_o - S_o^0 \end{cases} \quad (9)$$

where D_i and D_j are the average optical densities for wavelengths i and j, respectively, and S_w and S_o are the water and the NAPL saturations, respectively, corresponding to time $= t$. D_i^0, D_j^0, S_w^0, and S_o^0 are the initial conditions corresponding to time $= 0$. Since D_i, D_j, D_i^0, D_j^0, S_w^0, and S_o^0 are known, Eq. (8) can then be used to calculate S_w and S_o at any point in the domain.

SIMPLIFIED IMAGE ANALYSIS METHOD

The Multispectral Image Analysis Method relies on the employment of different band-pass filters, which are flat by design in order to allow digital cameras to capture photographs of the light reflected by the studied system at particular wavelengths. Since these band-pass filters are typically designed for parallel light, in the case of photography, their behavior depends on the angle of incidence of the light reflected by a subject. As shown in Fig. 5, the angle of incidence varies from one extreme to the other for the same subject. Although the example herein is one-dimensional, the same principles apply for two-dimensional cases.

The effect is also clearly visible when plotting the optical density matrix for a domain with constant saturation at all points (Fig. 6). In this example, a Toyoura sand column, fully saturated with water, is analyzed at both 450 nm and 640 nm, and the radial pattern clearly demonstrates the problem described in Fig. 5 for a two-dimensional case. Although this problem can be resolved using a specific tailor-made curved band-pass filter, the solution is cost prohibitive (for reference, a standard 52-mm flat visible light band-pass filter costs around 5,000 Japanese yen, whereas a tailor-made 72-mm filter costs 30,000 Japanese yen or six times that amount).

It should be noted that during the tests, the relative position between the camera and the studied domain remains constant, and consequently, the various angles of incidence of the reflected light when passing through a band-pass filter (Fig. 5) also remain constant throughout the tests. Hence, we can assume that there are dozens of small (and different) band-pass filters at fixed positions, instead of only one filter in front of the camera (Fig. 7).

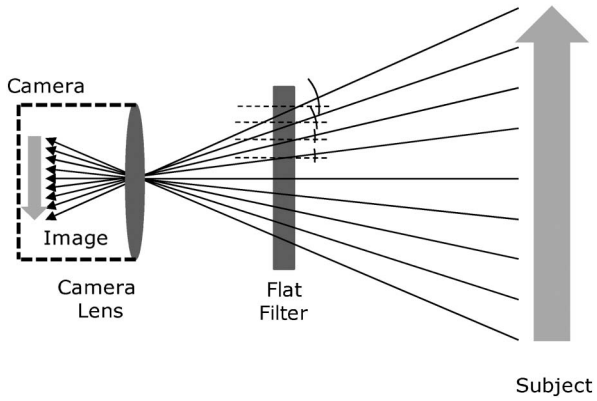

Fig. 5 Variable angle of incidence of reflected light on flat band-pass filters

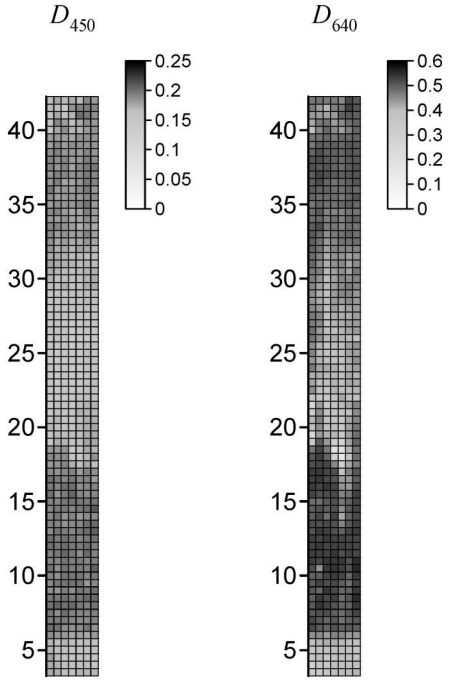

Fig. 6 Effect of variable angle of incidence of reflected light on optical density matrices

Fig. 7 Due to variable angle of incidence of light, band-pass filter behaves as dozens of small band-pass filters connected to each other

This means that we would need to prepare a different set of calibration equations for each small assumed band-pass filter. As the mesh used in Fig. 6 has 490 elements ($m \times n = 70 \times 7$) and the improved calibration method described by Flores et al. (2009b) used 148 different samples to produce a single set of calibration equations, we would need a total of 23,520 different samples to produce the 490 different sets of calibration equations required here, which is impractical. Therefore, there is a need to develop a simplified version of the Multispectral Image Analysis Method.

Remembering that each Eq. (7) represents a plane, and three non-collinear points are needed to define a plane, carefully selecting points will provide the necessary planes (i.e., set of equations) for each mesh element. In our case, the best points are those located in the extremes of the plane (Fig. 8). This means

1) $S_w = 0\%$; $S_o = 0\%$ Dry sand
2) $S_w = 0\%$; $S_o = 100\%$ Sand fully saturated with LNAPL
3) $S_w = 100\%$; $S_o = 0\%$ Sand fully saturated with water

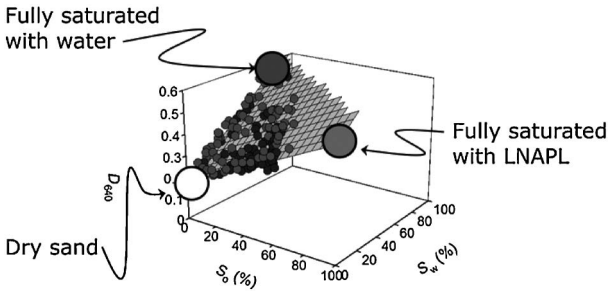

Fig. 8 Regression plane can be defined with three extreme points. Plotted data from Flores et al. (2009b)

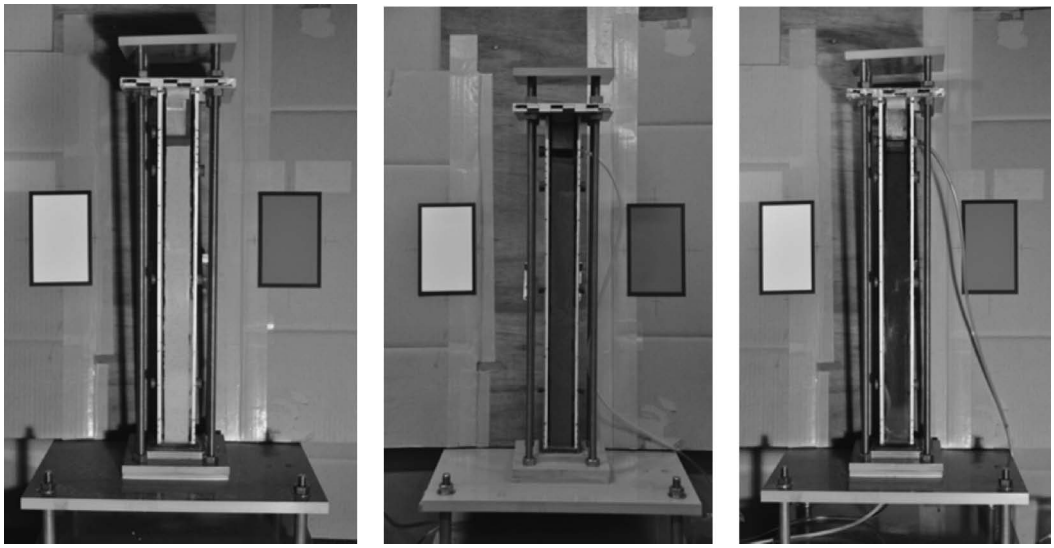

Fig. 9 Left: Column filled with dry sand; Center: Column filled with fully water-saturated sand; Right: Column filled with fully LNAPL-saturated sand

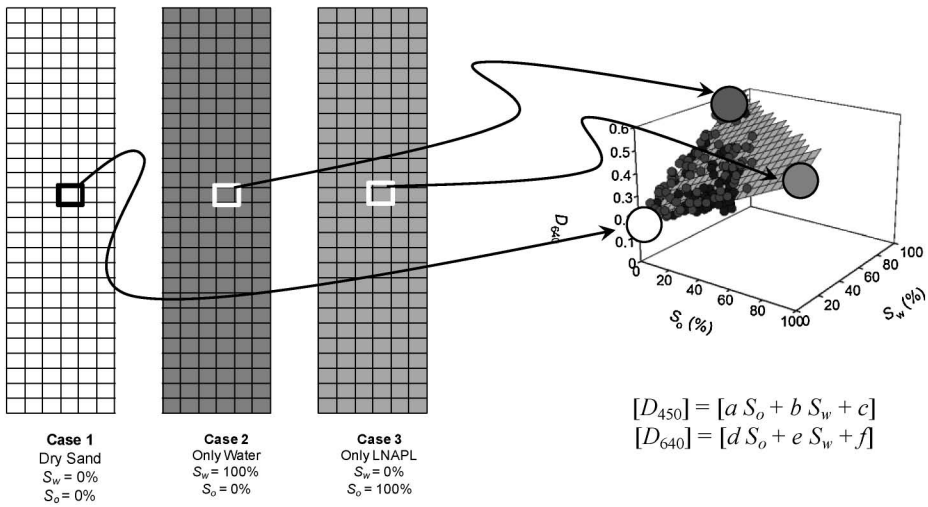

Fig. 10 Each mesh element yields unique set of regression equations

It is relatively easy to photograph each element of the matrix under these three limit conditions, because all we need to do is to fill the domain with sand for each situation and all the elements will share the same condition (Fig. 9). Then, we can calculate the average optical density values for each mesh element, compare these values to the corresponding ones for all three cases, and obtain a matrix of correlation equation sets where each set corresponds to a mesh element (Fig. 10).

Each photograph will yield a different average optical density matrix $[D_i^{00}]_{mn}$, $[D_i^{10}]_{mn}$, and $[D_i^{01}]_{mn}$ for pictures taken with band-pass filter i, and $[D_j^{00}]_{mn}$, $[D_j^{10}]_{mn}$, and $[D_j^{01}]_{mn}$ for pictures taken with band-pass filter j. These optical density matrices can be combined to yield not a single pair of correlation equations, but a matrix of correlation equations where each pair corresponds to a mesh element:

$$\begin{bmatrix} D_i \\ D_j \end{bmatrix}_{mn} = \begin{bmatrix} (D_i^{10} - D_i^{00}) \cdot S_w + (D_i^{01} - D_i^{00}) \cdot S_o + D_i^{00} \\ (D_j^{10} - D_j^{00}) \cdot S_w + (D_j^{01} - D_j^{00}) \cdot S_o + D_j^{00} \end{bmatrix}_{mn} \quad (10)$$

where m and n are the vertical and the horizontal dimensions of the matrix, $[D_i]_{mn}$ and $[D_j]_{mn}$ are the values of the average optical density of each mesh element for wavelengths i and j, respectively. $[D_i^{00}]_{mn}$ and $[D_j^{00}]_{mn}$ are the average optical density of each mesh element for dry sand. $[D_i^{10}]_{mn}$ and $[D_j^{10}]_{mn}$ are those for water-saturated sand, while $[D_i^{01}]_{mn}$ and $[D_j^{01}]_{mn}$ are those for NAPL-saturated sand. Since each mesh element has its own pair of correlation equations that accounts for the variable behavior of the band-pass filters, the spatial variation in light, and the effects of the glass wall, image subtraction is unnecessary. Thus, one potential source of error can be eliminated.

GENERAL PROCEDURE

The procedure for calculating the water and NAPL saturation values on full domains subjected to dynamic conditions can be divided into three phases, namely, calibration, experiment, and computational analysis, as described below.

Calibration

1) Fill the experimental domain with oven-dried sand ($S_w = 0\%$, $S_o = 0\%$).
2) Take two simultaneous pictures of the domain, one picture with each camera.
3) Fill the experimental domain with water-saturated sand ($S_w = 100\%$, $S_o = 0\%$).
4) For a second time, take two simultaneous pictures of the domain, one picture with each camera.
5) Fill the experimental domain with LNAPL-saturated sand ($S_w = 0\%$, $S_o = 100\%$).
6) For a third time, take two simultaneous pictures of the domain, one picture with each camera.

Experiment

1) Fill the experimental domain with sand under the desired initial conditions.
2) Initiate the drainage/imbibition/migration process.
3) Take two simultaneous pictures of the domain, one picture with each camera, at the desired frequency.
4) Finish the experiment.

Computational Analysis

1) Calculate the $[D_i^{00}]_{mn}$, $[D_i^{10}]_{mn}$, $[D_i^{01}]_{mn}$, $[D_j^{00}]_{mn}$, $[D_j^{10}]_{mn}$, and $[D_j^{01}]_{mn}$ matrices from the pictures acquired during the Calibration phase.
2) Calculate the matrix of the correlation equations.
3) Calculate the matrices of average optical densities $[D_i]_{mn}$ and $[D_j]_{mn}$ from the pictures taken during the Experiment phase.
4) Calculate saturation matrices $[S_w]_{mn}$ and $[S_o]_{mn}$ by solving the correlation equations obtained in Step 2 after replacing the average optical densities obtained in Step 3.

WATER DRAINAGE TEST

Equipment and Materials

A one-dimensional column, $3.5 \times 3.5 \times 50$ cm, with a transparent glass wall (Fig. 11) was designed to study the behavior of the falling groundwater table in a one-dimensional column of Toyoura sand (particle density $\rho = 2.65$ g/cm^3, equivalent grain size $D_{60} = 0.196$, and void ratio $e = 1.1$) with the aid of the Simplified Image Analysis Method. This setup was used for all calibration pictures and tests, so that the glass wall could be kept constant and present in all pictures. This column and the tests are similar to those by Kamon et al. (2007), but the column was square (3.5×3.5 cm) instead of circular ($\phi = 3.5$ cm) to minimize the optical distortion when taking digital photographs.

A consumer grade digital camera (Nikon D70s) with a 450-nm band-pass filter was used to photograph the column. The sole lighting sources were two 500 W flood-

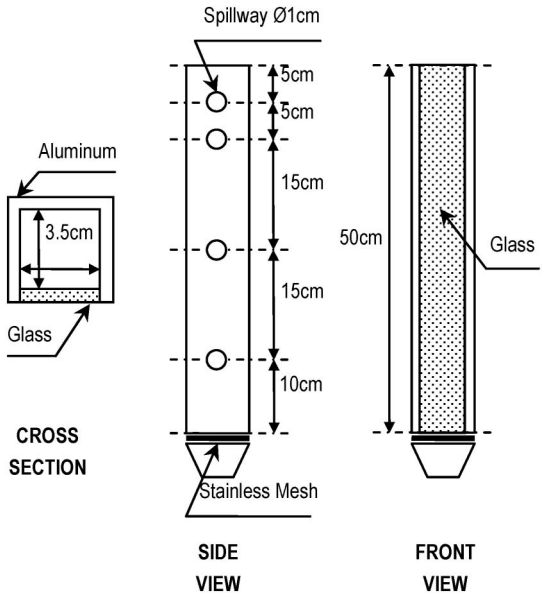

Fig. 11 Column design

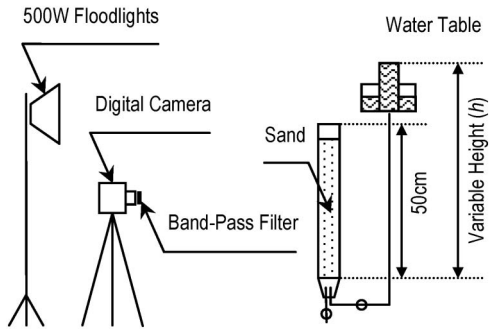

Fig. 12 Column system design

lights in a dark room, and a Gretagmacbeth white balance card was located next to the column to provide a constant white reference. An external water tank was connected to the column to control the height of the water table (Fig. 12). To facilitate the observations, the water was dyed blue with Brilliant Blue FCF (1:10000), a dye that neither migrates from water to paraffin liquid nor is adsorbed by the soil particles.

Calibration

This test only required two calibration photographs, namely, the column filled with dry sand and the column filled with water-saturated sand (left and center of Fig. 9, respectively). As only water was used, we can focus on one side of the regression plane ($S_o = 0\%$) shown in Fig. 8. Hence, Eq. (10) can be reduced to

$$[D_{450}]_{mn} = [(D^{10}_{450} - D^{00}_{450}) \cdot S_w + D^{00}_{450}]_{mn} \quad (11)$$

where m and n are the dimensions of the matrix. $[D_{450}]_{mn}$ is the value of the average optical density of each mesh element for the 450-nm wavelength. $[D^{00}_{450}]_{mn}$ is the average optical density of each mesh element for the dry sand, while $[D^{10}_{450}]_{mn}$ is the average optical density of each mesh element for the water-saturated sand.

Experiment

The column was initially filled with fully water-saturated Toyoura sand. The sand was previously saturated with the blue-dyed water and left overnight in a vacuum chamber to ensure complete saturation. Then, with the help of a spoon, the saturated sand was slowly poured into the column filled with de-aired water and compacted with an aluminum bar every 2–3 cm. The external water tank, initially located at $h = 45$ cm, was quickly lowered to $h = 5$ cm, and the water inside the column was drained for 60 hours. To avoid producing a vacuum, the top of the column was left open. Digital pictures were taken every hour. The camera was set to manual mode, and the aperture, the shutter speed, and the white balance were defined and maintained constant throughout the experiment. The camera was remotely controlled (using Nikon Camera Control Pro 2 software) to avoid vibrations and camera displacement. The two 500-W floodlights were turned on 30 seconds prior to taking the pictures and then turned off right afterwards to avoid fluctuations in the column's temperature. The room temperature was kept at 20°C and the humidity at 70% (Table 1).

Table 1. Description of water drainage column tests

	Time	Water head	Comments
Initial condition	0 hr	45 cm	Water-saturated column
Drainage	0 hr→60 hr	5 cm	

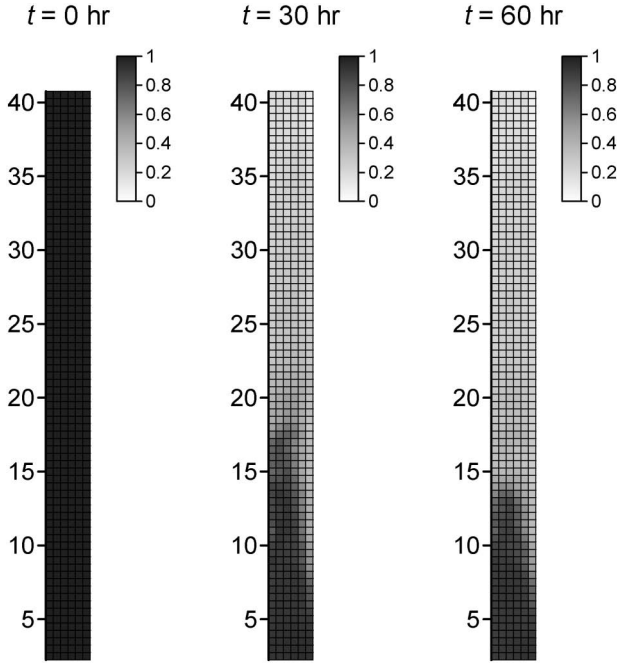

Fig. 13 Water saturation distribution matrices $[S_w]_{mn}$ for $t = 0$, 30, and 60 hr for Water Drainage Test

Computational Analysis

All pictures were exported from the NEF format (Nikon proprietary RAW version files) to the TIFF format (Tagged Image File Format) using Nikon ViewNX 1.5.0. TIFF images were analyzed with an ad-hoc program written in MATLAB ver. 2007a to obtain $[D_{450}]_{mn}$.

As previously mentioned, because NAPL was not infiltrated during this test, $S_o = 0\%$, and the simplified Eq. (11) was used, where $[D^{00}_{450}]_{mn}$ and $[D^{10}_{450}]_{mn}$ are the average optical density matrices calculated from the two calibration pictures (left and center pictures in Fig. 9). $[D_{450}]_{mn}$ is calculated for each picture taken during the test so that water saturation matrix $[S_w]_{mn}$, which corresponds to each picture, can be solved. Figure 13 plots the $[S_w]_{mn}$ values for $t = 0$, 30, and 60 hr.

Although Fig. 13 shows the water distribution for the entire domain at three specific instances during the experiment ($t = 0$, 30, and 60 hr), we obtained 61 similar water distribution graphics in all (not shown here), because data was collected every hour throughout the 60-hour test. Instead of showing all 61 pictures, we analyzed the dynamic behavior of the water column by examining a Water saturation vs. Time plot for areas of the column

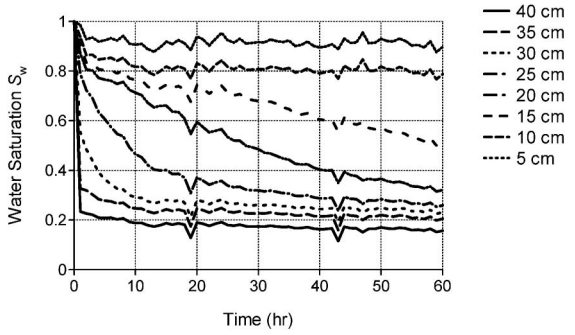

Fig. 14 Water saturation vs. Time at different heights for Water Drainage Test

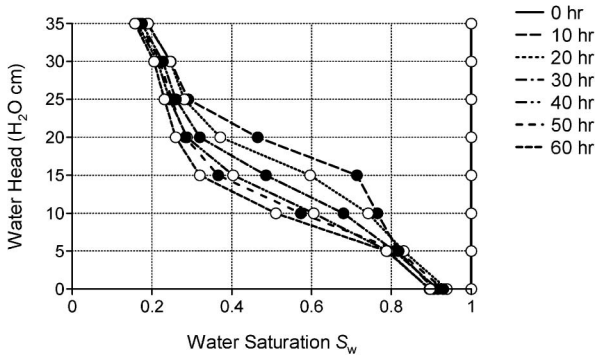

Fig. 15 Variation in *S-p* relation with time for Water Drainage Test

Table 2. Drained water mass balance, comparison of calculated and measured values

Water in the column	Real	Computed
W_w at $t=0$ hr	NA	216.68 g
W_w at $t=60$ hr	NA	88.51 g
Drained water	117.45 g	128.17 g
Difference (mass)	10.72 g	
Difference (%)	9.1%	

located at different heights (Fig. 14). Each line in Fig. 14 corresponds to the behavior of the water saturation in the column at a specific height with time. Figure 15 plots the saturation-water head pairs corresponding to $t=0$, 10, 20, 30, 40, 50, and 60 hr. Using the saturation distribution profiles obtained by the Simplified Image Analysis Method, the masses of water present within the column at $t=0$ and 60 hr were estimated. By calculating the difference between these two masses, it was inferred that 128.17 g of water drained out of the column. In fact, 117.45 g were recovered from the external tank, yielding a difference of 9.1% (Table 2).

Discussion

The first experiment tested the Simplified Image Analysis Method for a two-phase case (air/water). The lack of the third phase allowed Eq. (10) to be simplified, but the overall method remained the same. Similar to previous experiments (data not shown), the image analysis method is extremely sensitive to variations in lighting conditions; thus, efforts were made to maintain constant conditions.

Figure 13 depicts the water distribution inside the column at three different times, and shows that despite our efforts to create a uniformly compacted volume of sand, preferential paths were created at the corners of the square-shaped cross section of the column (Fig. 11), which are apparent because the water front receded more quickly from the center of the column. Although this is undesirable behavior, it illustrates how the Simplified Image Analysis Method is capable of showing differences in water saturation by calculating the saturation distribution for the entire domain with high detail, especially compared to other methods (e.g., electrical conductivity probe and gamma-ray attenuation) that measure saturation at specific points, typically along the center, and assume that the saturation front recedes uniformly with height.

Figure 14 shows the dynamic behavior of water with time as well as how the receding water front is displaced faster at the beginning of the experiment and then slowly stabilizes. Once the water saturation (S_w) approached 15%, it remained there for the duration of the experiment. This value is called Residual Saturation, and the value for the most extreme condition (when $h=40$ cm) of 15.7%, is close to that obtained by Li (2005), which was 14.5% for an air-water system following the van Genuchten model. Figure 15 shows the displacement of the saturation-water head relation, which is close to the *S-p* relation, with time. The larger the water head, the faster a stabilized condition was achieved.

Finally, although the difference between the calculated amount of water that drained from the column (obtained using our simplified method) and the real amount of water recovered was less than 10%, because the external tank, which recovered the drained water, was open to the room during the 60-hour experiment, it is possible that some of the water evaporated. This would be possible even under the controlled temperature and humidity conditions maintained in the room. Thus, the real difference may be less than the calculated 9.1%. To reduce this potential error, two measures were taken in the subsequent experiment: (i) a closed system was employed to minimize the amount of evaporation from the drained water and (ii) paraffin liquid, a non-volatile LNAPL for the mass-balance comparison fluid, was used.

WATER-LNAPL DRAINAGE AND IMBIBITION TEST

Equipment and Materials

This test employed the same one-dimensional column designed for the water drainage test (Fig. 11) as well as a similar system setup (Fig. 12). Like the two-phase test, the porous medium was Toyoura sand and the wetting fluid was the same blue-dyed water (Brilliant Blue FCF, 1:10000). However, this test used a second consumer grade digital camera (Nikon D80) with a 640-nm bandpass filter. The non-wetting fluid was red-dyed paraffin

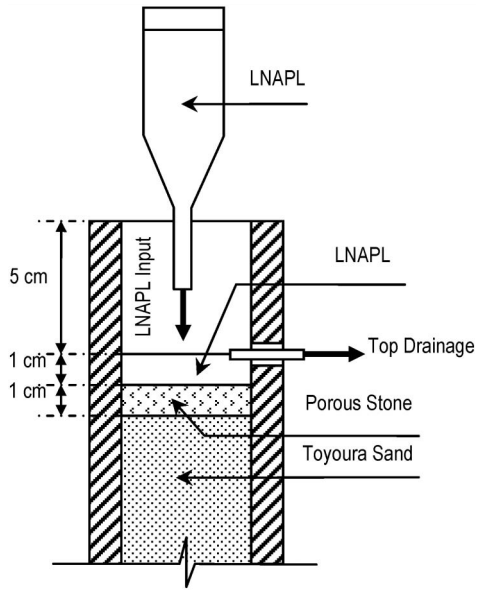

Fig. 16 Setup of top part of column for Water-LNAPL Drainage and Imbibition Test

liquid (Sudan III, 1:10000), an LNAPL. Brilliant Blue FCF dye does not migrate from water to paraffin liquid, while Sudan III dye does not migrate from paraffin liquid to water. Additionally, neither dye is adsorbed by the soil particles.

A specific setup was devised for the top part of the column to keep it fully saturated during the first hour of the test (Fig. 16).

Calibration

This test required three calibration pictures with each camera, namely, a picture was taken with each camera of the column filled with dry sand, the column filled with water-saturated sand, and the column filled with LNAPL-saturated sand (Fig. 9). These six pictures correspond to $[D^{00}_{450}]_{mn}$, $[D^{10}_{450}]_{mn}$, $[D^{01}_{450}]_{mn}$, $[D^{00}_{640}]_{mn}$, $[D^{10}_{640}]_{mn}$, and $[D^{01}_{640}]_{mn}$.

The values of matrices $[D^{00}_{450}]_{mn}$, $[D^{10}_{450}]_{mn}$, $[D^{00}_{640}]_{mn}$, and $[D^{10}_{640}]_{mn}$, for the water-LNAPL drainage and imbibition test, are the same as those corresponding to the water drainage test, so the same pictures were used for both experiments. In order to be able to do this, all environmental conditions (position of the lights, temperature, humidity, camera settings, etc.) had to be the same for both experiments, and great care was taken to make the two columns as similar as possible (same sand, same packing procedure, etc.)

Experiment

For this experiment, the column was filled with fully water-saturated Toyoura sand, but this time it was topped with a 1 cm cap of LNAPL. Prior to being added to the column, the sand was saturated with the blue-dyed water and left overnight in a vacuum chamber to ensure that it was completely saturated. Then, with the help of a spoon, the sand was slowly poured into the column filled with de-aired water and compacted with an aluminum bar every 2–3 cm. The test was divided into four stages, namely, first drainage ($t = 0$ to 72 hr), first imbibition ($t =$ 72 to 120 hr), second drainage ($t = 120$ to 192 hr), and second imbibition ($t = 192$ to 240 hr).

Table 3. Description of water-LNAPL drainage and imbibition column test

	Time	Water head	Comments
Initial condition	0 hr	45 cm	Water-saturated column
First drainage	0 hr→1 hr	−20 cm	28 g LNAPL infiltration
	1 hr→72 hr	−20 cm	
First imbibition	72 hr→120 hr	92 cm	
Second drainage	120 hr→192 hr	−20 cm	
Second imbibition	192 hr→240 hr	92 cm	

First Drainage. The water tank was quickly lowered 65 cm from its original position to a height of $h = -20$ cm (20 cm below the bottom of the column), and the water inside the column was allowed to drain. During the first hour of the test, 28 g of LNAPL infiltrated the column from the top through the porous stone. Beginning in the second hour, air was allowed to freely infiltrate the column through the same porous stone. The top of the column was left open to avoid producing a vacuum effect. This stage took 72 hours.

First Imbibition. After the end of the first drainage, the water tank was quickly raised 112 cm to a height of $h = 92$ cm, and due to rise in water pressure, the water table inside the column rose. The LNAPL that infiltrated into the column during the drainage process was displaced by the water and flowed out of the column through the top spillway. The top of the column was left open to avoid the occurrence of overpressure. This stage took 48 hours.

Second Drainage. The water tank was lowered again to $h = -20$ cm, and the water and the LNAPL present in the column were allowed to drain. No additional LNAPL infiltrated into the column. This stage took 72 hours.

Second Imbibition. The water tank was raised once again to a height of $h = 92$ cm, and both water and the remaining LNAPL rose due to the rising water pressure. The excess water and the LNAPL flowed out of the column through the top spillway. This stage took 48 hours.

Two digital pictures of the column were taken simultaneously every hour using two cameras, one picture with a 450-nm band-pass filter and the other with a 640-nm band-pass filter. Both cameras were set to manual mode, and all the pictures were acquired with the same aperture, shutter speed, and white balance settings as the previous test. Similar to the Water Drainage Test, both cameras and the 500-W floodlights were remotely controlled to avoid vibrations, displacement, and changes in the temperature of the column. The room temperature was also maintained at 20°C and the humidity at 70% (Table 3).

Computational Analysis

Similar to the previous test, all the pictures were ex-

ported from the NEF format to the TIFF format, and then they were analyzed with an ad-hoc program written in MATLAB ver. 2007a.

Using the six calibration pictures, the average optical density matrices, $[D^{00}_{450}]_{mn}$, $[D^{10}_{450}]_{mn}$, $[D^{01}_{450}]_{mn}$, $[D^{00}_{640}]_{mn}$, $[D^{10}_{640}]_{mn}$, and $[D^{01}_{640}]_{mn}$, were calculated. The following matrix of correlation equations was obtained:

$$\begin{bmatrix} D_{450} \\ D_{640} \end{bmatrix}_{mn} = \begin{bmatrix} (D^{10}_{450} - D^{00}_{450}) \cdot S_w + (D^{01}_{450} - D^{00}_{450}) \cdot S_o + D^{00}_{450} \\ (D^{10}_{640} - D^{00}_{640}) \cdot S_w + (D^{01}_{640} - D^{00}_{640}) \cdot S_o + D^{00}_{640} \end{bmatrix}_{mn} \quad (12)$$

$[D_{450}]_{mn}$ and $[D_{640}]_{mn}$ were calculated for each picture taken during the test, and the water and LNAPL saturation matrices ($[S_w]_{mn}$ and $[S_o]_{mn}$), which correspond to each picture following the aforementioned procedure, were solved. Figures 17 and 18 plot the $[S_w]_{mn}$ and $[S_o]_{mn}$ values for $t = 0$, 72, 120, 192, and 240 hr for the first and second drainage and imbibition cycles, respectively.

Since the water and LNAPL saturation values do not necessarily total 100%, it would be impossible to plot them together in the same graph. Thus, the column with time is represented by two graphs in Figs. 17 and 18, namely, the graphs on the left represents LNAPL saturation distribution $[S_o]_{mn}$ and the graphs on the right represents water saturation distribution $[S_w]_{mn}$. Each pair should be considered together when studying the state of the column at a given time. The dynamic behaviors of both the water and the LNAPL fronts can be better understood if S_w and S_o are plotted with time (Figs. 19 and 20).

According to the image analysis, after the two drainage and imbibition cycles of the original 28.00 g infiltrated during the first hour, 4.95 g of LNAPL remained in the column. Thus, 23.05 g should have been displaced out of the column. In fact, 22.02 g were recovered from the external tank, a difference of 4.7% (Table 4).

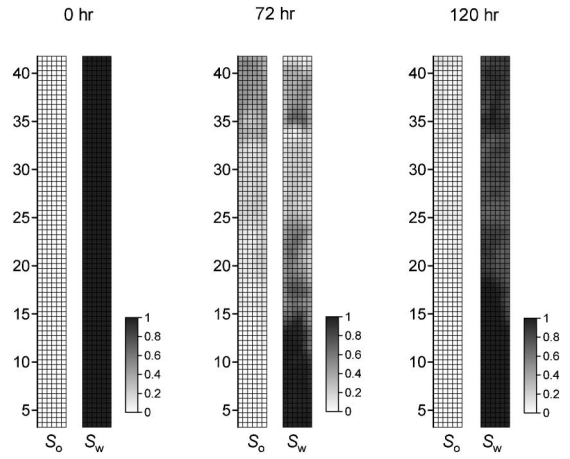

Fig. 17 First drainage and imbibition. Left plots correspond to water saturation matrices $[S_w]_{mn}$ and right plots to LNAPL saturation matrices $[S_o]_{mn}$ for Water-LNAPL Drainage and Imbibition Test

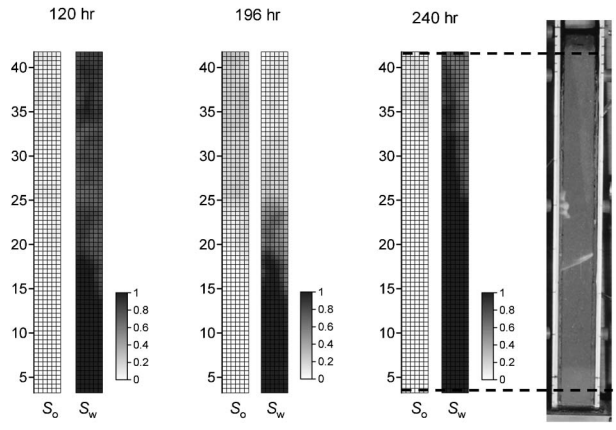

Fig. 18 Second drainage and imbibition. Left plots correspond to water saturation matrices $[S_w]_{mn}$ and right plots to LNAPL saturation matrices $[S_o]_{mn}$ for Water-LNAPL Drainage and Imbibition Test

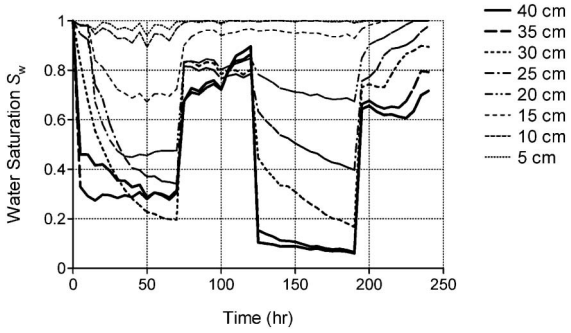

Fig. 19 Water saturation vs. Time for Water-LNAPL Drainage and Imbibition Test

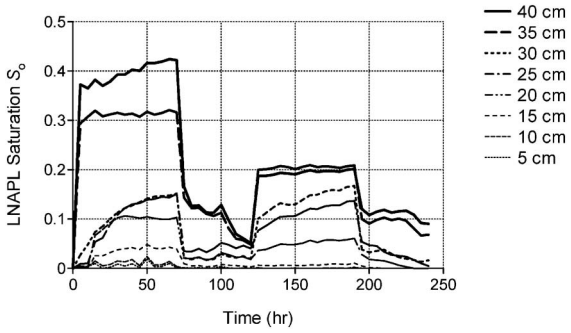

Fig. 20 LNAPL saturation vs. Time for Water-LNAPL Drainage and Imbibition Test

Table 4. Drained LNAPL mass balance, comparison between calculated and measured results

LNAPL in the column	Real	Computed
W_o at $t = 0$ hr	0.00 g	0.00 g
W_o at $t = 1$ hr	28.00 g	NA
W_o at $t = 240$ hr	NA	4.95 g
Drained LNAPL	22.02 g	23.05 g (28.00–4.95)
Difference (mass)		1.03 g
Difference (%)		4.7%

As an optical comparison, Fig. 18 shows $[S_o]_{mn}$ and $[S_w]_{mn}$ matrices corresponding to $t = 240$ hr side by side as well as a color picture of the column taken at the end of the experiment.

Discussion

This second experiment tested the Simplified Image Analysis Method for the three-phase case (air/water/LNAPL) under a more complex fluctuating condition. Figures 17 and 18 show that the method can perceive and calculate minute amounts of LNAPL, which are not easily observed with the naked eye. The paraffin liquid showed typical LNAPL behavior under imposed fluctuating conditions; it initially migrated downward following the draining water until it reached a stable condition, and then it remained on the top part of the column even though the water table was 15–20 cm lower (Fig. 17, $t =$ 72 hr). During the imbibition stage, raising the water table displaced part of the LNAPL, but some remained trapped within the column even though it should have floated over the water table (which was 50 cm above LNAPL), because LNAPL is less dense than water (Fig. 17, $t = 120$ hr). The second drainage-imbibition cycle displayed the same behavior, and by the end of the experiment (Fig. 18, $t = 240$ hr), nearly 5 g or 18% of the original infiltrated 28 g remained trapped within the column below the water table.

The difference between the calculated amount of displaced LNAPL and the actual recovered LNAPL was only 4.7%, which is less than half the difference observed in the first test. This apparent improvement in accuracy is most likely due to the non-volatile characteristic of paraffin liquid, which suggests that because the conditions within the column were not altered (we only improved the reception of the drained water), the error of the method when calculating the water and LNAPL saturation distribution within the column is actually close to 5%.

Figure 19 shows the dynamic variation in water saturation with time for different heights within the column. The results indicate a pattern similar to that reported by Li (2005), namely, that the water dropped quickly during the first hours of each drainage process and then stabilized at values close to the limit conditions of the corresponding LNAPL-Water *S-p* relation. That is, the saturation of water for 40-cm capillary heads was near 20%, while that for 20-cm capillary heads was near 50% and that for capillary heads less than 20-cm exceeded 80%.

Discrepancies in the saturation values between the ones reported here and the ones reported by Li (2005) are mainly due to two different experimental conditions, namely, (i) because Li's column used an electrical conductivity probe as a saturation measurement method, Li's column was designed to be only two-phase (Water-LNAPL), whereas the column herein is a three-phase (Air-Water-LNAPL) and (ii) the position of the water table varied from 45 cm→5 cm→74.3 cm→5 cm→74.3 cm for Li's column, and yet that described herein varied from 45 cm→ −20 cm→92 cm→ −20 cm→92 cm. The latter reason is less important than the former, because capillary pressure values greater than 40 cm yield the same water saturation values (Residual Saturation).

Due to the ability of the Simplified Image Analysis Method to assess both water and LNAPL saturation distributions for the entire domain under the dynamic conditions studied in this test, the migration of LNAPL could be observed throughout the domain. Therefore, our results differ from those of other experiments, such as ones carried out by Li (2005), which could only monitor water and/or LNAPL saturation at a single point within the studied domain. From the analysis of the graphics for both Water saturation vs. Time and LNAPL saturation vs. Time (Figs. 19 and 20), we are able to observe their behavior with time. For example, we found that the LNAPL reached a height of $h = 15$ cm during the first drainage stage, but only reached $h = 20$ cm during the second drainage, whereas the saturation of LNAPL at $h = 40$ cm and 35 cm were 40% and 30%, respectively, during the first drainage, but only 20% for both cases during the second drainage. These observations clearly demonstrate that LNAPL penetrates less during the second drainage stage due in part to being pushed out of the column during the first imbibition stage. Additionally, by observing that in the second drainage, the water saturation values were lower for heights $h = 35$ and 40 cm, but $h = 15$ and 20 cm had higher saturation values, it is clear that the presence of a contaminant that can be displaced by the water table (i.e., LNAPL), affects the behavior of the water by increasing its mobility. Although not measured for this experiment, this behavior is consistent with the lower values of pore pressure of the *S-p* relation for water-LNAPL compared to the one corresponding to air-water (Li, 2005).

As a final note, we would like to comment that, while the experiments conducted for this study were performed with an LNAPL, the basic theories can be applied for all NAPLs in general, which means that the Simplified Image Analysis Method introduced in this paper can be used not only to study the behavior of LNAPLs, but also that of DNAPLs in the subsurface under complex three-phase conditions.

CONCLUSIONS

In this study, we developed and tested a novel Simplified Image Analysis Method to assess water and LNAPL saturation distributions in porous media subjected to fluctuating groundwater. The results indicate that this method is well suited for studying the behavior of LNAPL migration in the subsurface under controlled dynamic laboratory conditions.

This new method accounts for the effects of the variable angle of incidence of reflected light, which affect the response of band-pass filters that is not addressed by the Multispectral Image Analysis Method, while simultaneously eliminating the need to prepare dozens of samples for the calibration stage. In addition to improving the accuracy for points far from the center, this new simplified

method saves time and laboratory resources because time-consuming calibrations are unnecessary.

The new simplified method requires only three calibration pictures, which are acquired using two cameras, and the filling of the studied domain with sand under the following three limit conditions: (i) dry sand ($S_w = 0\%$; $S_o = 0\%$), (ii) water-saturated sand ($S_w = 100\%$; $S_o = 0\%$), and (iii) LNAPL-saturated sand ($S_w = 0\%$; $S_o = 100\%$). These three conditions represent the three limits of the regression calibration equations, which have been shown to be planes, and produce the limit values of the average optical density for each mesh element. Additionally, because the domain used for the calibration pictures is used in subsequent experiments, the spatial variations in light, small scratches on the surface of the domain, and other imperfections, which require image subtraction in the Multispectral Image Analysis Method, are unnecessary. Thus, potential sources of error are eliminated.

The Simplified Image Analysis Method increases the mathematical complexity of the computational analysis, because one set of equations is provided for each mesh element instead of a set of regression equations for the entire domain. This increased complexity improves the accuracy of the method by providing each mesh element with its own set of non-related equations, which account for both spatial variations in light and other surface imperfections.

To test the feasibility of the Simplified Image Analysis Method to yield both water and LNAPL saturation distributions for the entire domain, we conducted two different laboratory experiments to test the suitability when subjected to fluctuating groundwater conditions. The devised experiments tested two different conditions, namely, (i) a column subjected to a falling water table without LNAPL infiltration and (ii) a column subjected to two cycles of water table drainage and imbibition after being contaminated by an LNAPL. These two conditions allowed us to test the method for two-phase (air/water) and three-phase (air/water/LNAPL) systems. The Simplified Image Analysis Method measured both water and LNAPL saturation distributions under these dynamic conditions with a reasonable margin of error, which tended to be on the conservative side (larger saturation values than the actual ones) due to the wall effect. Paraffin liquid showed typical LNAPL behavior under the imposed dynamic conditions in the three-phase test, in other words, initially it migrated downward due to gravitational forces until it reached a somewhat stable condition, and from there it was vertically displaced by the capillary zone of the rising water table.

The ability of the Simplified Image Analysis Method to assess both water and LNAPL saturation distributions throughout the entire domain under the dynamic conditions in these experiments allowed us to observe the displacement of water and LNAPL during the tests. By comparing the displacements for the first drainage/imbibition cycle with the second one, their different types of behavior were elucidated. The behavior is consistent with lower values for pore pressure in the S-p relation for water-LNAPL compared to that corresponding to the air-water, as presented by Li (2005). In general, the Simplified Image Analysis Method is capable of calculating both water and LNAPL distribution saturation values for domains subjected to dynamic conditions in both vertical and horizontal directions, and can be an invaluable tool when running several different laboratory experiments to study the fate of LNAPLs in subsurface water.

ACKNOWLEDGMENTS

The research presented in this paper was supported by the Japan Society for the Promotion of Science (JSPS) through a Grant-in-Aid for Scientific Research (Grant No. 19360212) and by the Ministry of Education, Culture, Sports, Science and Technology (MEXT) through a post-graduate scholarship awarded to the first author.

REFERENCES

1) Darnault, C. J. G., Throop, J. A., DiCarlo, D. A., Rimmer, A., Steenhuis, T. S. and Parlange, J. Y. (1998): Visualization by light transmission of oil and water contents in transient two-phase flow fields, *Journal of Contaminant Hydrology*, **31**(3–4), 337–348.
2) DiCarlo, D. A., Bauters, T. W. J., Steenhuis, T. S., Parlange, J.-Y. and Bierck, B. R. (1997): High-speed measurements of three-phase flow using synchrotron X rays, *Water Resources Research*, **33**(4), 569–576.
3) Flores, G., Inui, T., Katsumi, T., Takatsukasa, Y. and Kamon, M. (2009a): Improvement of the precision of the image analysis method used as a tool to study LNAPL migration in porous media, *Proceedings of the International Joint Symposium on Geodisaster Prevention and Geoenvironment in Asia (JS-Fukuoka 2009)*, Fukuoka, 216–221.
4) Flores, G., Inui, T., Katsumi, T., Takatsukasa, Y. and Kamon, M. (2009b): Mechanism of geoenvironmental contamination with LNAPLs at sites close to the ocean, *Proceedings of 19th International Offshore and Polar Engineering Conference*, Osaka, Japan, **2**, 323–329.
5) Gold, A. and Asher, J. B. (1976): Soil reflectance measurement using a photographic method, *Soil Sci. Soc. Am. J.*, **40**, 337–341.
6) Høst-Madsen, J. and Jensen, K. H. (1992): Laboratory and numerical investigations of immiscible multiphase flow in soil, *Journal of Hydrology*, **135**(1–4), 13–52.
7) Iizuka, K. (1987): *Engineering Optics*, Springer-Verlag, New York.
8) Kamon, M., Endo, K. and Katsumi, T. (2003): Measuring the k-S-p relations on DNAPLs migration, *Engineering Geology*, **70**(3–4), 351–363.
9) Kamon, M., Li, Y., Endo, K., Inui, T. and Katsumi, T. (2007): Experimental study on the measurement of S-p relations of LNAPL in a porous medium, *Soils and Foundations*, **47**(1), 33–45.
10) Kechavarzi, C., Soga, K. and Wiart, P. (2000): Multispectral image analysis method to determine dynamic fluid saturation distribution in two-dimensional three-fluid phase flow laboratory experiments, *Journal of Contaminant Hydrology*, **46**(3–4), 265–293.
11) Kiely, G. (1998): *Environmental Engineering*, Irwin/McGraw-Hill, Singapore.
12) Li, Y. (2005): Mechanism of LNAPL migration in conjunction with groundwater fluctuation, *Doctoral Thesis*, Kyoto University, 167.
13) MacAdam, D. L. (1981): *Color Measurement, Theme and Variations*, Springer-Verlag, New York.
14) Rimmer, A., DiCarlo, D. A., Steenhuis, T. S., Bierck, B., Durnford, D. and Parlange, J. Y. (1998): Rapid fluid content measurement method for fingered flow in an oil-water-sand system using synchrotron X-rays, *Journal of Contaminant Hydrology*, **31**(3–4), 315–335.

15) Schincariol, R. A., Herderick, E. E. and Schwartz, F. W. (1993): On the application of image analysis to determine concentration distributions in laboratory experiments, *Journal of Contaminant Hydrology*, **12**(3), 197–215.
16) Sharma, R. S. and Mohamed, M. H. A. (2003): An experimental investigation of LNAPL migration in an unsaturated/saturated sand, *Engineering Geology*, **70**(3–4), 305–313.
17) Skoog, D. A., Holler, F. J. and Crouch, S. R. (2007): *Principles of Instrumental Analysis*, Thomsom Brooks/Cole, Belmont.
18) Tilley, R. J. D. (2003): *Colour and Optical Properties of Materials: An Exploration of the Relationship Between Light, the Optical Properties of Materials and Colour*, John Wiley & Sons, Ltd, West Sussex.
19) Tuck, D. M., Bierck, B. R. and Jaffe, P. R. (1998): Synchrotron radiation measurement of multiphase fluid saturations in porous media: Experimental technique and error analysis, *Journal of Contaminant Hydrology*, **31**(3–4), 231–256.
20) Van Geel, P. J. and Sykes, J. F. (1994): Laboratory and model simulations of a LNAPL spill in a variably-saturated sand, 1. Laboratory experiment and image analysis techniques, *Journal of Contaminant Hydrology*, **17**(1), 1–25.
21) Van Genuchten, M. T. (1980): A closed-form equation for predicting the hydraulic conductivity of unsaturated soils, *Soil Science Society of America Journal*, **44**(5), 892–898.